Electronic Supplementary Material (ESI) for ChemComm.

Cation Etching Induced Deep Self-Reconstruction to Form Polycrystalline Structure for Efficient Electrochemical Water Oxidation

Jing Zhang,[b] Jing Guo,[c] Hugang Li,[a] Hao Luo,[d] and Shuai Niu[a,*]

[a] Laboratory of Ecology-based Solutions, College of Ecology, Taiyuan University of Technology, Taiyuan 030024, China

[b] School of Chemistry and Materials Science of Shanxi Normal University, Taiyuan 031000, China

[c] School of Physics and Information Engineering, Shanxi Normal University, Taiyuan 031000, China

[d] School of Chemistry and Chemical Engineering, Hefei University of Technology, Hefei 23009, China

[*] Corresponding authors: niushuai@tyut.edu.cn

Experimental Section

Chemicals: All chemical reagents were analytical (AR) grade and were used as received without further purification. Nickel foam (labeled as NF) was purchased from Kunshan Kuangxun Electrical Co., Ltd. ruthenium(III) chloride, sodium chloride, ammonium molybdate tetrahydrate, nickel nitrate hexahydrate, sodium hydroxide, RuO_2 nanoparticles were obtained from Alfa Aesar. Ethanol and acetone were purchased from Beijing Chemical Works. Milli-Q deionized water (resistance of 18.2 MΩ cm at 25 °C) were used for all experiments.

Preparation of Ru-Ni(OH)$_2$/NF: NF (2×3 cm^2) was ultrasonically cleaned in ethanol, acetone, and deionized water for 30 min before use. Typically, Ru-Ni(OH)$_2$/NF was synthesized via hydrothermal methods with a simple modification. First, NaCl and $RuCl_3$ with different molar ratios (n=0, 0.05, 0.25, 1) were dissolved in 30 mL of deionized water under magnetic stirring to form the homogeneous solutions. After stirring for 30min, the obtained solutions were transferred into a Teflon-lined steel autoclave (50 mL) and then maintained at 80 °C for 6 h. Then, the products are naturally cooled to room temperature. The obtained solid products were washed several times with deionized water and ethanol solution, and the products were collected through centrifugation. Finally, the products were dried under vacuum at 60°C for 12 h. The catalyst was denoted as Ru-Ni(OH)$_2$/NF.

Preparation of NiRu-OH/NF: The NiRu-OH/NF was obtained by in situ electrochemical oxidizing of Ru-Ni(OH)$_2$/NF in 1 M KOH solution at a constant current density, such as 100 mA cm^{-2} for 0.5 h, 1 h, 2 h and 3h; and 200 mA cm^{-2} for 1 h.

Preparation of Ni(OH)$_2$/NF: A piece of pretreated NF was placed in a Teflon-lined stainless autoclave (50 mL) containing 15 mL NaOH (5 mol/L) solution. The autoclave was sealed and maintained at 80 °C for 6h. After the autoclave cooled down slowly to room temperature, the sample was taken out and washed with deionized water before thoroughly drying.

Preparation of MoNi$_4$/MoO$_2$/NF: A piece of pretreated NF was placed into 15 mL solution containing 0.04 M $Ni(NO_3)_2{\cdot}6H_2O$ and 0.01 M $(NH_4)_6Mo_7O_{24}{\cdot}6H_2O$. in a Teflon autoclave. The $NiMoO_4$/NF was obtained by hydrothermal methods in a Teflon-lined steel autoclave (50 mL) and then maintained at 150 °C for 6 h. After naturally cooling to room temperature and washing with DI water, the $NiMoO_4$ cuboids were achieved on the NF ($NiMoO_4$/NF). Finally, $NiMoO_4$/NF was annealed at 500 °C for 2 h in a H_2/Ar (v/v, 10/90) atmosphere to achieve $MoNi_4/MoO_2$/NF.

Characterization: The morphology of products was taken by a scanning electron microscopy (SEM) (a Hitachi S-4800, Japan) operated at 15 kV. The microstructure of products was performed by a transmission electron microscopy (TEM) (JEM-2100F, Japan) operated at an acceleration voltage of 200 kV. The corresponding elemental distribution analyses (EDS) was collected on an energy dispersive X-ray spectrometer (EDX) (Oxford Materials Analysis) on the TEM. XPS was recorded on a Thermo Scientific ESCA Lab250xi using a Mg Kα X-ray as the excitation source. The binding energies were referenced to C 1s line at 284.8 eV from adventitious carbon. The crystalline structure was identified by powder X-ray diffraction patterns (XRD) on

Regaku D/Max-2500 diffractometer equipped with a Cu K α 1 radiation (λ=1.54056 Å).

Oxygen Evolution Reaction (OER) measurements: All electrochemical tests were conducted on an electrochemical workstation CHI 660E. All the overpotentials were given with 85% IR-compensation unless specified. Using a conventional three-electrode cell in 1.0 M KOH electrolyte. The as-prepared electrodes, Hg/HgO electrode (1.0 M KOH), and carbon rod were used as working electrode, reference electrode, and counter electrode, respectively. All measured potentials were converted to the reversible hydrogen electrode (RHE), according to the equation (1):

$$E_{RHE} = E_{Hg/HgO} + 0.098 + 0.059 * pH \qquad (1)$$

The linear sweep voltammetry (LSV) curves were recorded at a scan rate of 2 mV s^{-1}. All curves were recorded with 85% iR-compensation unless specified. The long-term stability test was performed using chronopotentiometry method at a constant current density. The C_{dl} values for as-prepared working electrodes were determined from the cyclic voltammogram (CV) in the double layer region (without faradaic processes) at different scan rates. Electrochemical impedance spectroscopy was carried out in a frequency range from 100 KHZ to 0.01 HZ and amplitude of 5 mV. For excluding the influence of ECSA on the performance, the OER performance was normalized by ECSA. The ECSA-normalized current density for as-prepared catalysts was calculated according to the equation (2):

$$\text{ECSA-normalized current density} = \text{current density} \times C_S/C_{dl} \qquad (2)$$

Here, C_S is the specific capacitance. In this work, 0.040 mF cm^{-2} was adopted as the value of C_S on a basis of previously reported OER catalysts in alkaline.

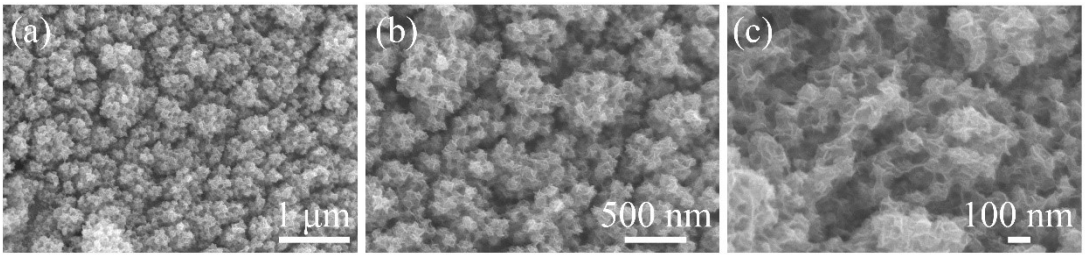

Fig. S1 The SEM images of Ru-Ni$(OH)_2$/NF with n=0.

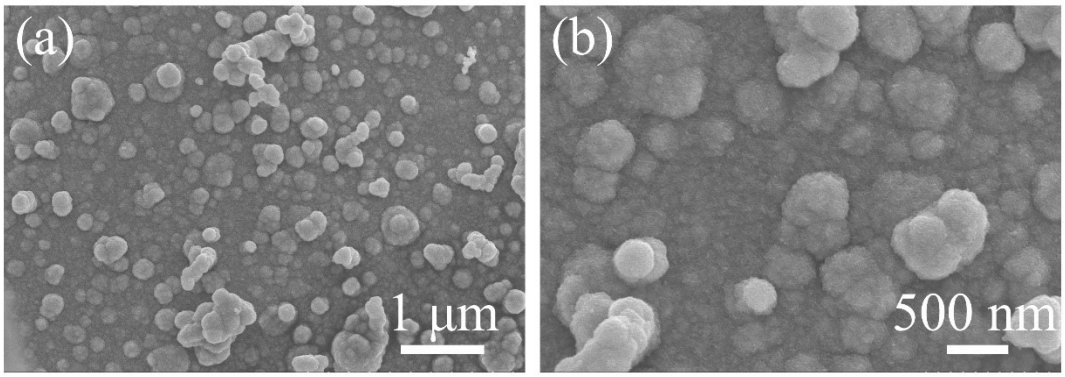

Fig. S2 The SEM images of Ru-Ni$(OH)_2$/NF with n=0.05.

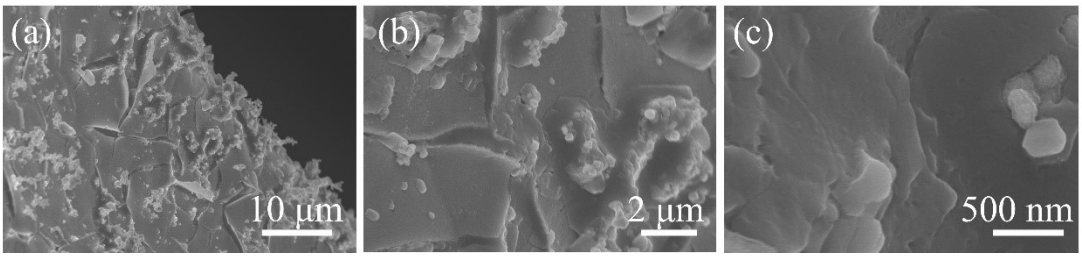

Fig. S3 The SEM images of Ru-Ni$(OH)_2$/NF with n=0.25.

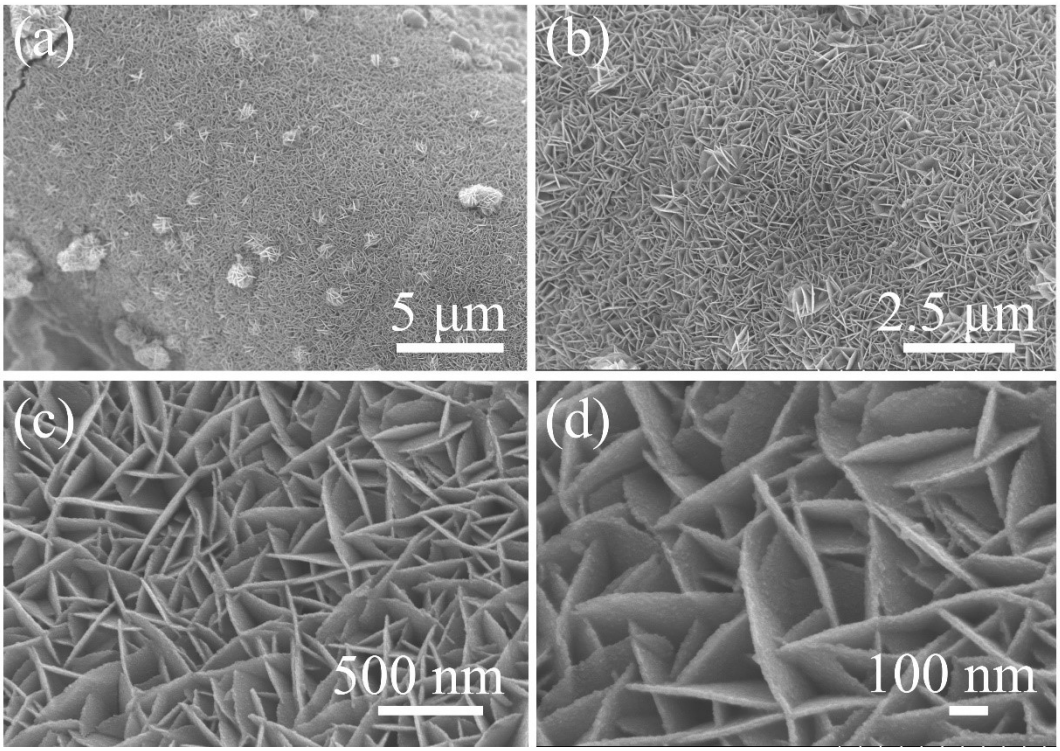

Fig. S4 The SEM images of Ru-Ni$(OH)_2$/NF with *n*=1.

The microstructure of Ru-Ni$(OH)_2$/NF is regulated by different molar ratios of NaCl and $RuCl_3$ (n=0, 0.05, 0.25, 1), which is conductive to improving catalytic activity. Firstly, the morphology of the product prepared by n=0 is nanoflowers, which is covered on the whole surface of NF (**Fig. S1**). Subsequently, as n gradually increases to 0.05, the nanoflowers begin to convert into agglomerated nanospheres on NF (**Fig. S2**). After that, the Ru-Ni$(OH)_2$/NF layer uniformly covers the whole surface of NF when n increases to 0.25 (**Fig. S3**). Until n increases to 1, the Ru-Ni$(OH)_2$ layer is composed of an array of vertically grown nanosheets with rough surfaces (**Fig. S4**).

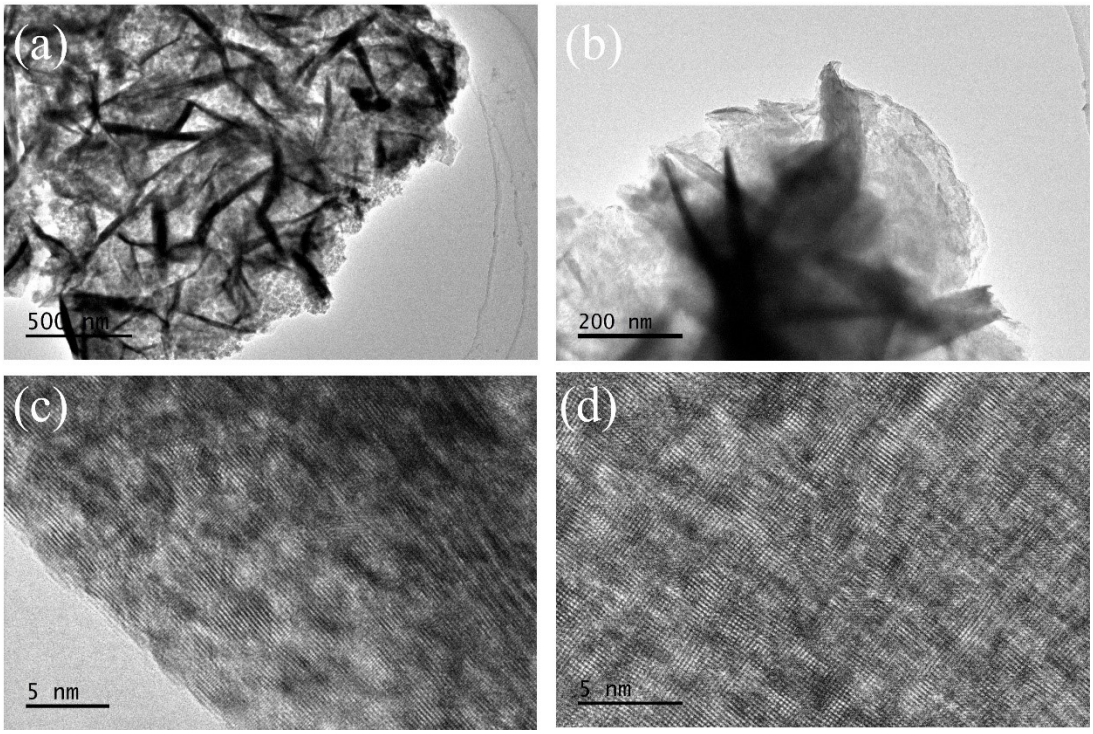

Fig. S5 The TEM images of Ru-Ni$(OH)_2$/NF with n=1.

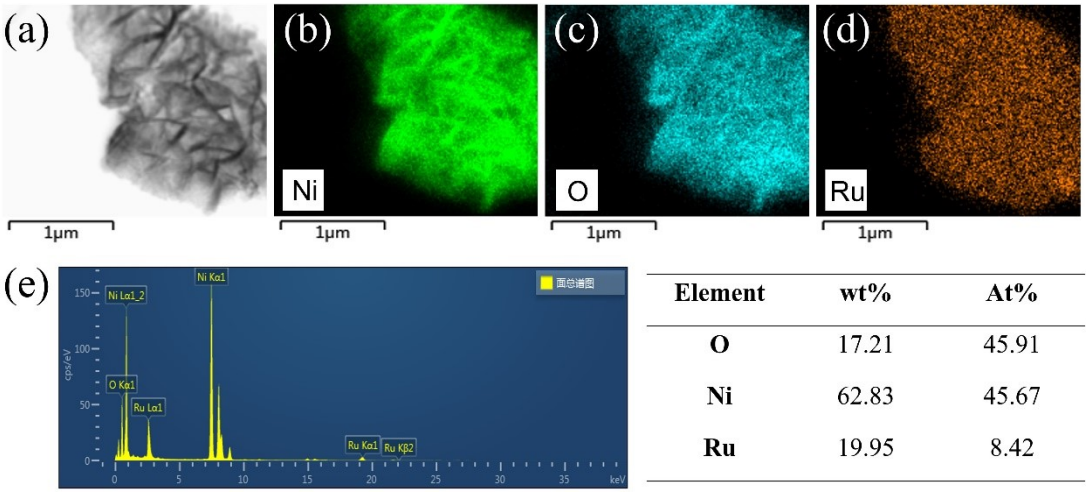

Element	wt%	At%
O	17.21	45.91
Ni	62.83	45.67
Ru	19.95	8.42

Fig. S6 (a) TEM image and (b-d) corresponding elemental mapping images, and (e) EDS spectrum of Ru-Ni$(OH)_2$/NF with n=1.

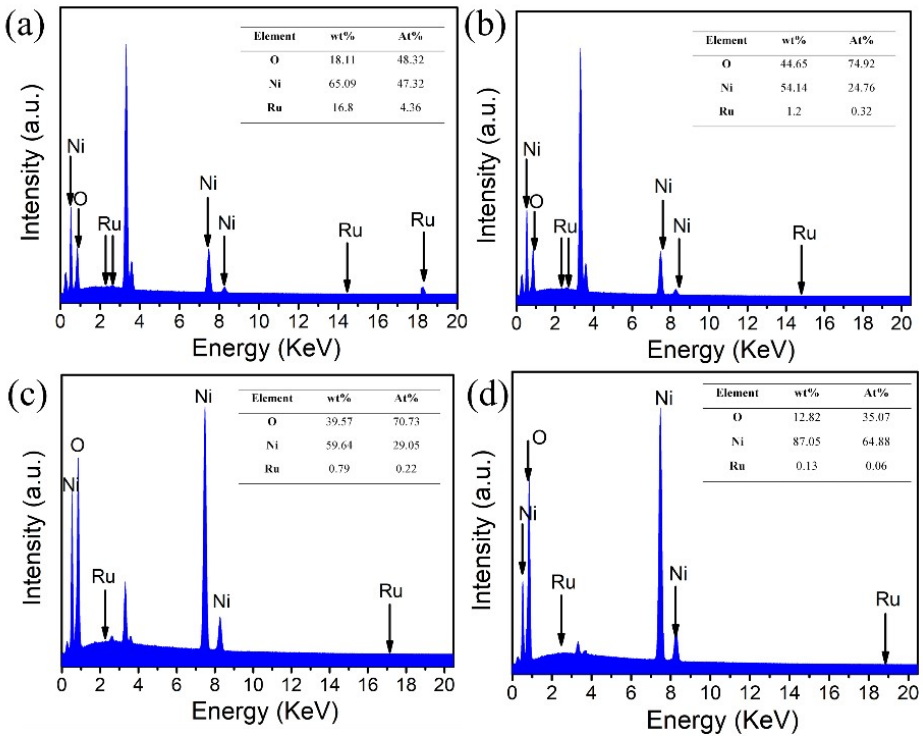

Fig. S7 The EDS spectrum of RuNi-OH/NF under different leaching time at the current of 100 mA cm^{-2} for (a) 0.5 h, (b) 2 h, (c) 3 h, respectively, and (d) 1 h at 200 mA cm^{-2}.

A series of catalysts were prepared by controlling the leaching time to obtain the saturated atom content of Ru. Meanwhile, the compositions of products prepared at different conditions were analysed by EDS as shown in the following **Fig. S7.** Overall, it can be obviously detected that only Ni, Ru, and O elements distribute in the NiRu-OH/NF. Particularly, the content of Ru decreases with the leaching time, while the Ni content maintains a high level at the various leaching time. This result means that Ru atom in the Ru-$Ni(OH)_2$ is much easier to leach out by this strategy compared to that of Ni atom. Furthermore, the content of Ru sharply decreases at higher current densities, say 200 mA cm^{-2} for 1 h, indicating that the Ru atomic content saturate at the condition of 100 mA cm^{-2} for 1 h.

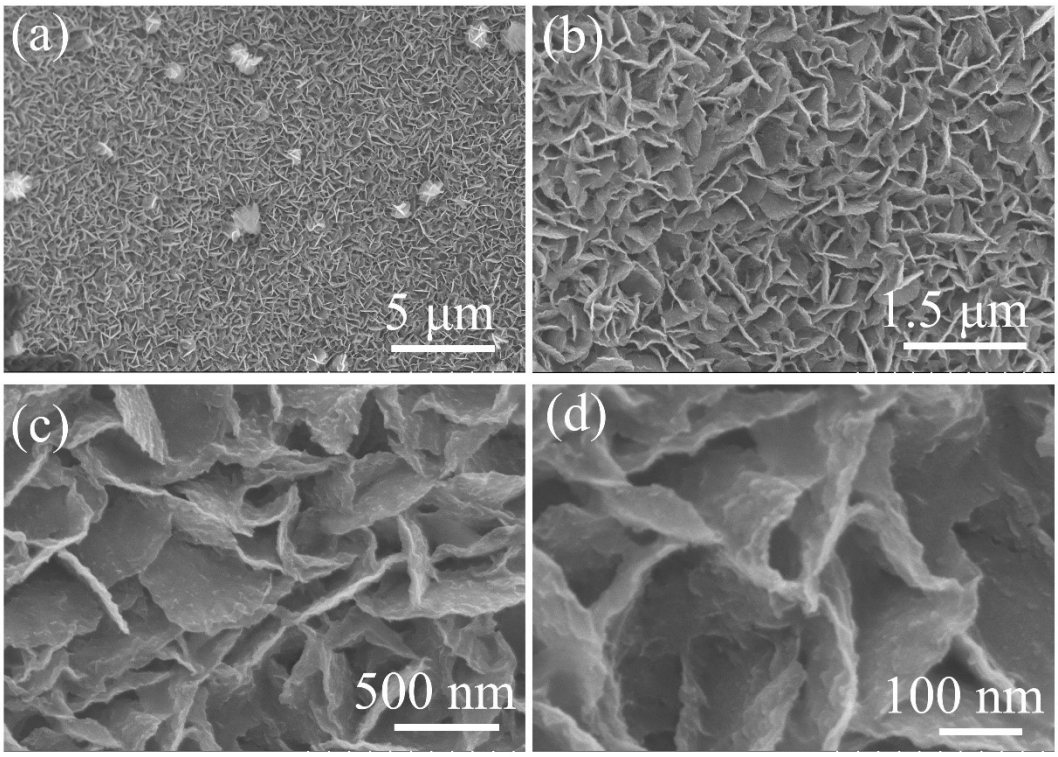

Fig. S8 The SEM images of NiRu-OH/NF.

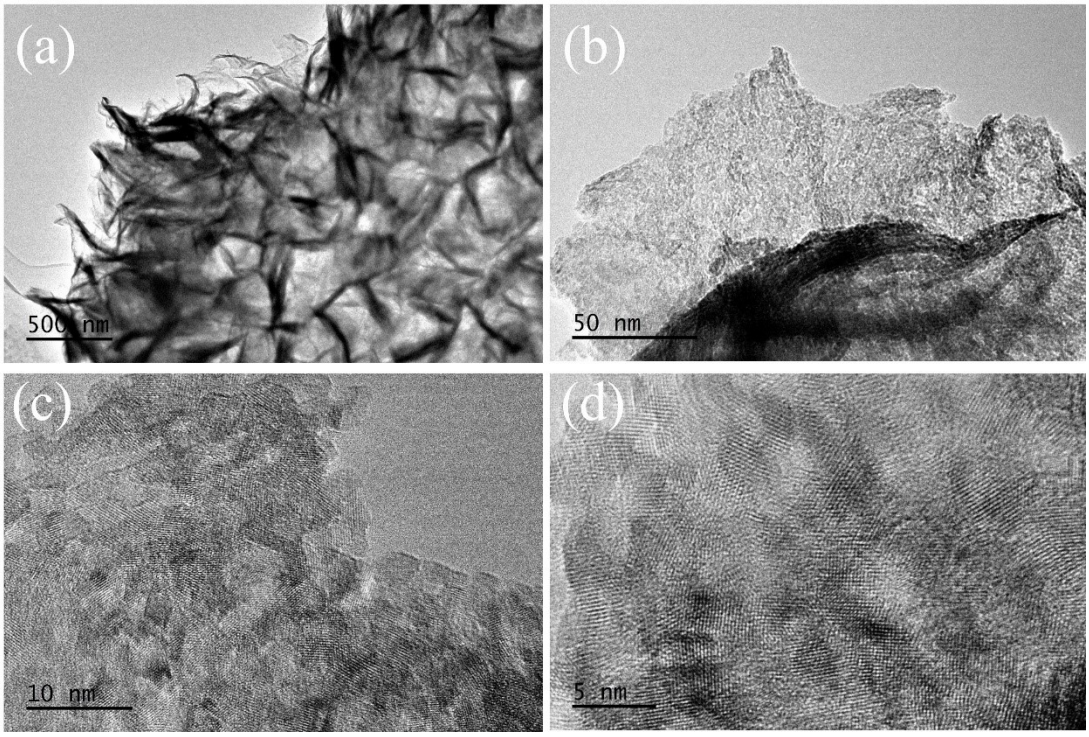

Fig. S9 The TEM images of NiRu-OH/NF.

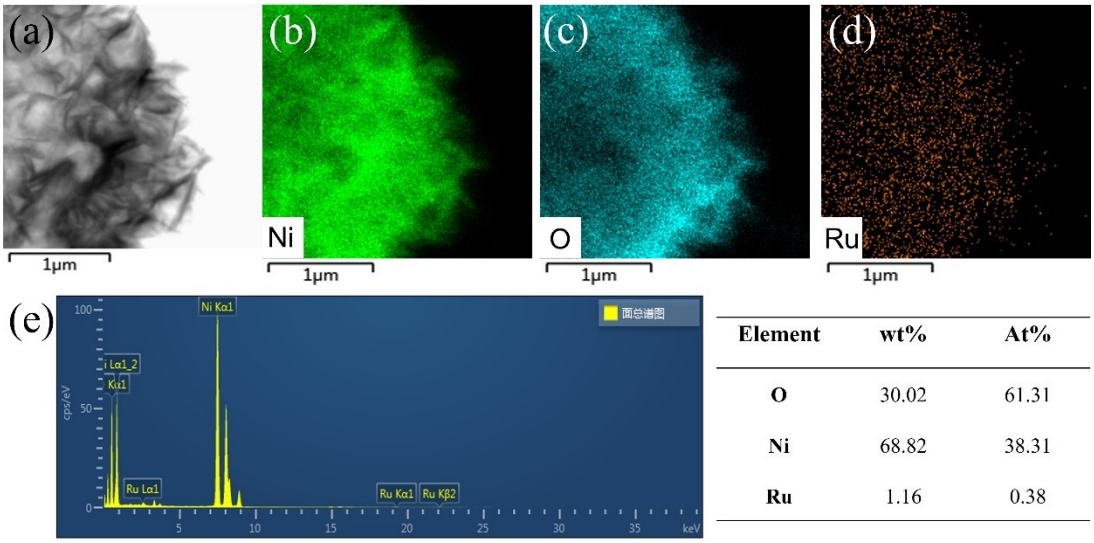

Element	wt%	At%
O	30.02	61.31
Ni	68.82	38.31
Ru	1.16	0.38

Fig. S10 (a) TEM image and (b-d) corresponding elemental mapping images, and (e) EDS spectrum of NiRu-OH/NF.

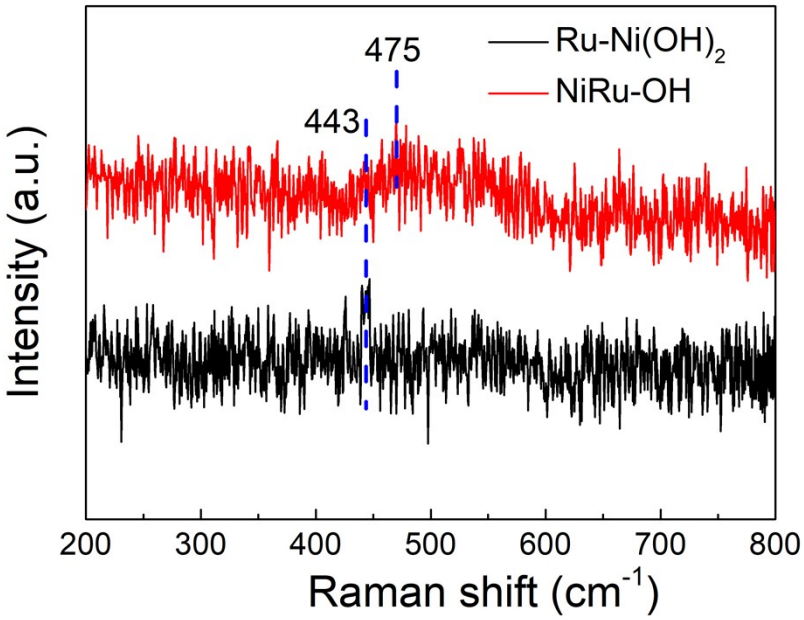

Fig. S11 The Raman spectra of Ru-Ni(OH)$_2$/NF and NiRu-OH/NF.

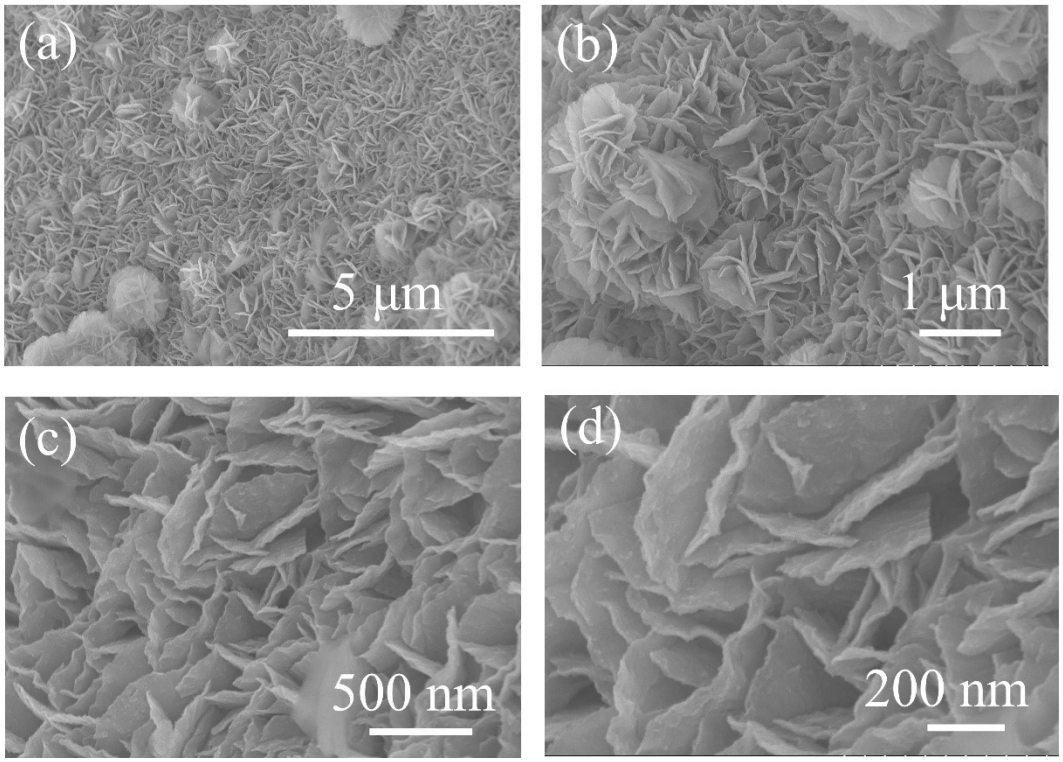

Fig. S12 The SEM images of NiRu-OH/NF after OER stability test.

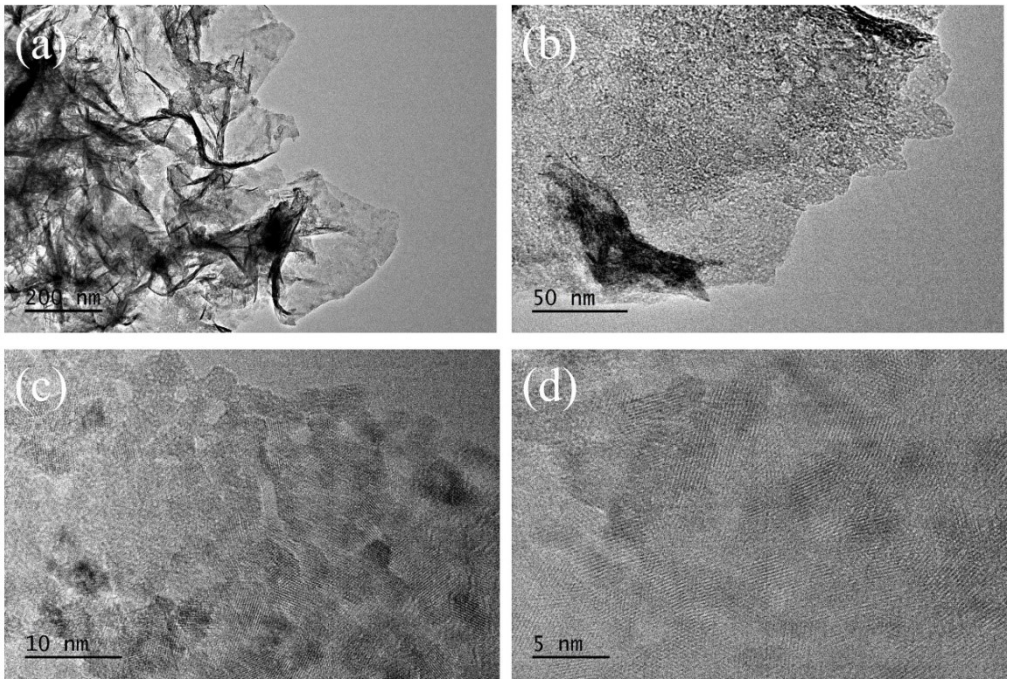

Fig. S13 The TEM images of NiRu-OH/NF after OER stability test.

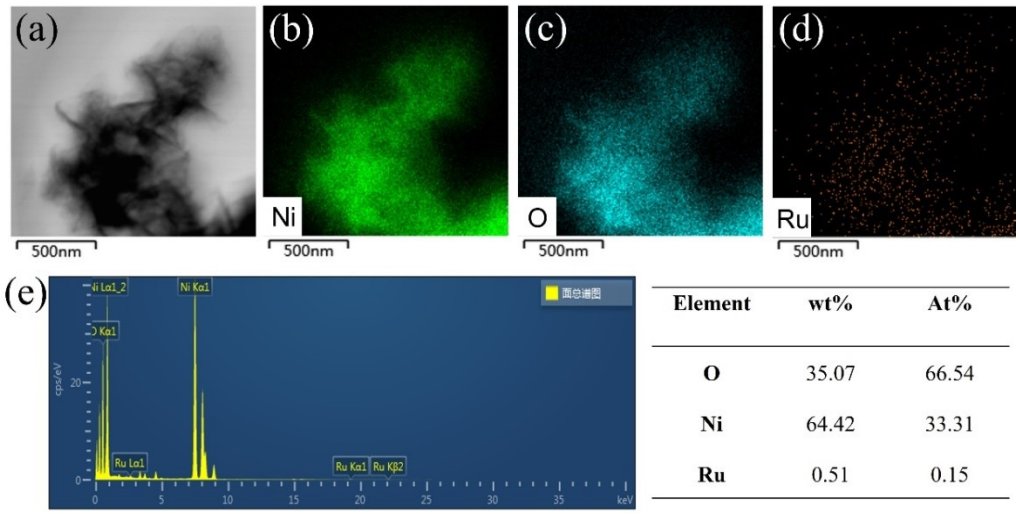

Element	wt%	At%
O	35.07	66.54
Ni	64.42	33.31
Ru	0.51	0.15

Fig. S14 (a) TEM image and (b-d) corresponding elemental mapping images, and (e) EDS spectrum of NiRu-OH/NF after OER stability test.

After the stability test, the SEM and TEM images of the catalyst evidence that there are still nanosheet arrays on NF and no obvious changes in morphology and structure (**Fig. S12 and 13**). More importantly, the elemental distribution of Ni and Ru are still uniformly evenly distributed across NF (**Fig. S14**). Besides, the atomic content of Ru slightly decreases after the stability test.

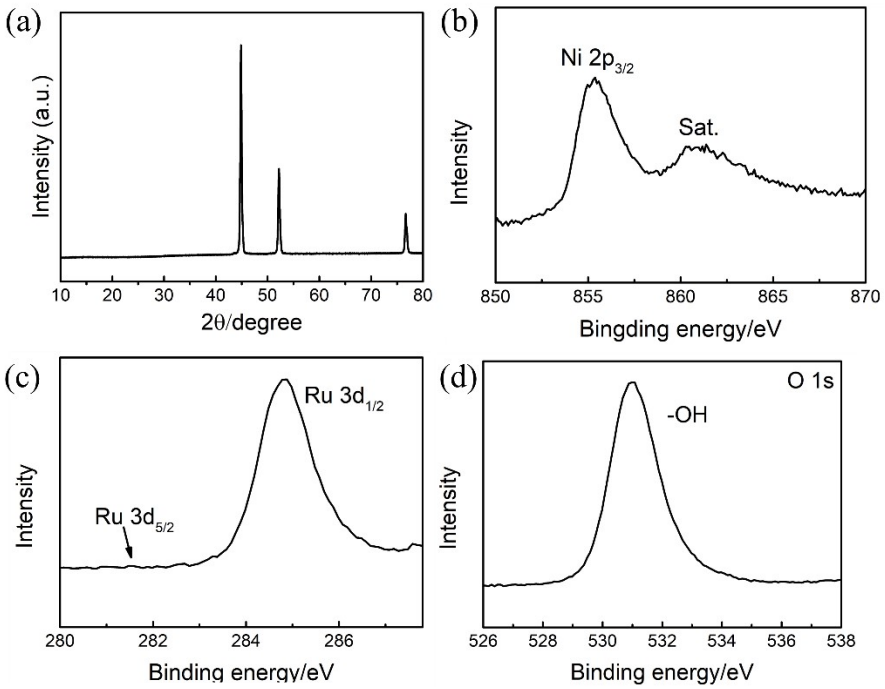

Fig. S15 (a) XRD patterns and high-resolution XPS spectra of (b) Ni 2p, (c) Ru 3d, and (d) O 1s of NiRu-OH/NF after stability test.

After the stability test, the XRD and XPS pattern of the catalyst after stability test were collected as shown in the **Fig. S15**. The XRD patterns only show the peak of Ni substrate, which indicates that the NiRu-OH nearly leached out from the sample during the OER test (**Fig. S15a**). Furthermore, XPS spectroscopies were further characterized after long-term stability testing. As shown in **Fig. S15b**, the peaks apart from the satellite peaks (labeled Sat.) are overlap of the doublets of Ni^{2+} and Ni^{3+} in Ni-based hydroxide. These results indicates that the original NiRu-OH should be oxidized into nickel (oxy)hydroxide or hydroxide during OER process, which are commonly observed as the OER active sites in the literatures. The Ru 3d XPS spectra show a doublet peaks at 281.3 eV and 284.8 eV, respectively, corresponding to Ru $3d_{5/2}$ and Ru $3d_{3/2}$ (**Fig. S15c**). Moreover, the O 1s peaks show a high peak at 531.3 eV, which is indicative of the -OH, which provides direct evidence for the hydroxide structure in all catalysts.

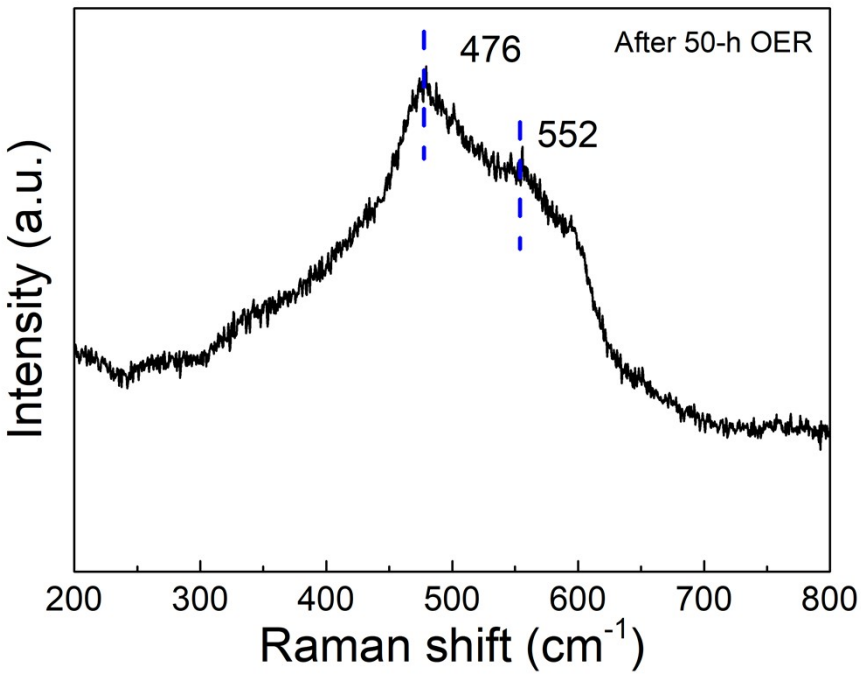

Fig. S16 The Raman spectra of NiRu-OH catalyst after 50 h OER stability.

Furthermore, its corresponding Raman spectrum exhibits NiOOH at 476 and 552 cm^{-1}, indicating the formation of more active NiOOH in NiRu-OH during the OER process (**Fig. S16**).

Table S1. Comparison of OER catalytic performance at in recent reports and this work in 1.0 M KOH.

Catalysts	Overpotential at 50 mA cm^{-2} (mV)	Overpotential at 100 mA cm^{-2} (mV)	Reference
NiRu-OH/NF	**286**	**321**	**This work**
NiFe-LDH@CS	292	372	Journal of Alloys and Compounds, **2023**, 941, 168994
Ni_3S_2/VG@NiCo-LDHs	--	320	Chem. Eng. J., **2021**, 415, 129048
NiCo-LDHs/NiCoS	--	308	Nano Res., **2022**, 15, 4986
Ni_3Fe@N-C	320	370	Advanced Powder Materials, **2022**, 1, 100020
NiFeB	316	350	Small **2022**, 18, 2203411
FeCo LDH/NF	--	338	Nano Res., **2022**, 15, 10021
CoNi/Zn(Fe,Al,Cr)$_2O_4$	--	335	Adv. Energy Mater. 2023, 2303450
(Fe,Co)OOH/MI	265	290	Adv. Mater. **2022**, *34*, 2200270
Rh/Ru-FeOOH@$Ti_3C_2T_x$	288	306	Small **2022**, 18, 2200173
Co-FeOOH-Ov/IF	285	296	Small **2023**, 19, 2301255

[1] D. Liu, Y. Yang, J. Zhang, L. Wang, Z. Ma, L. Ren, J. Wang, B. Xue, F. Li, Journal of Alloys and Compounds, **2023**, 941, 168994.

[2] X. Zhang, J. Fan, X. Lu, Z. Han, C. Cazorla, L. Hu, W. Tom, D. Chu, *Chemical Engineering Journal*, 2021, **415**, 129048.

[3] J. Li, L. Wang, H. He, Y. Chen, Z. Gao, N. Ma, B. Wang, L. Zheng, R. Li, Y. Wei, J. Xu, Y. Xu, B. Cheng, Z. Yin, D. Ma, Nano Res., 2022, **15**, 4986.

[4] Z. Li, X. Wu, X. Jiang, B. Shen, Z. Teng, D. Sun, G. Fu, Y. Tang, Advanced Powder Materials, 2022, **1**, 100020

[5] Y. Kang, Y. Guo, J. Zhao, B. Jiang, J. Guo, Y. Tang, H. Li, V. Malgras, Small **2022**, 18, 2203411

[6] T. Tang, Z. Jiang, J. Deng, S. Niu, Z.-C. Yao, W. Jiang, L.-J. Zhang, J. Hu, Nano Res., 2022, **15**,

10021.

[7] Y. Chen, J. Xu, M. Jiang, L. Wang, R. Ma, Y. Chen, Z.-H. Xie, P. Munroe, F. Hu, L. Li, S. Peng, Adv. Energy Mater. 2023, 2303450.

[8] W. Huang, J. Li, X. Liao, R. Lu, C. Ling, X. Liu, J. Meng, L. Qu, M. Lin, X. Hong, X. Zhou, S. Liu, Y. Zhao, L. Zhou, L. Mai, Adv. Mater. 2022, **34**, 2200270.

[9] B. Zhang, J. Shan, X. Wang, Y. Hu, Y. Li, Small 2022, **18**, 2200173.

[10] H.-J. Liu, S. Zhang, Y.-N. Zhou, W.-L. Yu, Y. Ma, S.-T. Wang, Y.-M. Chai, B. Dong, Small 2023, **19**, 2301255.